Stem Cell Reports
Report
OPEN ACCESS

Excitable Adult-Generated GABAergic Neurons Acquire Functional Innervation in the Cortex after Stroke

Timal S. Kannangara,[1,2,3,4] Anthony Carter,[1,4] Yingben Xue,[1] Jagroop S. Dhaliwal,[1,2,3] Jean-Claude Béïque,[1,2,3,4,*] and Diane C. Lagace[1,2,3,4,*]
[1]Department of Cellular and Molecular Medicine, Faculty of Medicine, University of Ottawa, Ottawa, ON K1H 8M5, Canada
[2]University of Ottawa Brain and Mind Research Institute, Ottawa, ON K1H 8M5, Canada
[3]Neuroscience Program, University of Ottawa, Ottawa, ON K1H 8M5, Canada
[4]Canadian Partnership for Stroke Recovery, Ottawa, ON K1G 5Z3, Canada
*Correspondence: jbeique@uottawa.ca (J.-C.B.), dlagace@uottawa.ca (D.C.L.)
https://doi.org/10.1016/j.stemcr.2018.10.011

SUMMARY

Ischemic stroke enhances the proliferation of adult-generated precursor cells that ectopically migrate toward the infarct. Studies have correlated precursor cell proliferation and subsequent adult neurogenesis with enhanced stroke recovery, yet it remains unclear whether stroke can generate new neurons capable of functional integration into the injured cortex. Here, using single and bitransgenic reporter mice, we identify spatial and temporal features of a multilineage cellular response to focal ischemia. We reveal that a small population of stroke-induced immature neurons accumulate within the peri-infarct region of the adult sensorimotor cortex, exhibit voltage-dependent conductances, fire action potentials, express GABAergic markers, and receive sparse GABAergic synaptic inputs. Collectively, these findings reveal that GABAergic neurons arising from the lateral ventricle have the capacity to integrate into the stroke-injured cortex, although their limited number and exiguous synaptic integration may limit their ability to participate in stroke recovery.

INTRODUCTION

Following an ischemic insult, regions surrounding the infarct, known as the peri-infarct region, respond with several forms of cortical plasticity, including dendritic remodeling (Brown et al., 2010), axonal sprouting (Dancause et al., 2005; Li et al., 2010b), and cortical remapping (Harrison et al., 2013). Running concurrent with these forms of plasticity is the enhanced proliferation of precursor cells (PCs) at the neurogenic niches, including the subventricular zone (SVZ) of the lateral ventricles (Zhang et al., 2004). Following a stroke, a significant population of PCs within the SVZ divert from their initial migration path and navigate toward the peri-infarct region, signifying a possible role for SVZ-derived PCs in post stroke recovery.

Investigation into the role of PCs after stroke, derived from loss-of-function studies that abolish the ischemia-driven PC response (Jin et al., 2010; Sun et al., 2013), suggests that PC proliferation is positively correlated with improved behavioral outcome (Lagace, 2012). Despite considerable effort examining this response, two essential features of ischemia-driven PCs remain unclear. First, it is unclear whether the ischemia-driven PC response solely gives rise to astrocytes (Benner et al., 2013; Parent et al., 2002; Shimada et al., 2010), or contains a neurogenic component (Kunze et al., 2015; Osman et al., 2011). While post-mortem studies identify adult-generated neurons in the stroke-injured cortex (Ekonomou et al., 2012; Jin et al., 2006), more recent work has suggested that adult-generated neurons are either absent or below detection levels (Carmichael, 2016; Huttner et al., 2014; Sorrells et al., 2018).

Second, if ischemia produces adult-generated neurons within the cortex, it is unknown whether these neurons functionally integrate into neural circuitry, a possible requisite to contribute to post stroke behavioral recovery (Lagace, 2012). Here, we determine the temporal and spatial dynamics of the multilineage cellular response to focal ischemia and demonstrate that adult-generated neurons become GABAergic neurons capable of limited integration in the cortex after a focal stroke.

RESULTS

Spatial and Temporal Multilineage Response from Nestin-GFP PCs following Ischemia

To investigate whether PCs generate functional neurons following stroke, we used Nestin-GFP mice (Yamaguchi et al., 2000) to label nestin-expressing (GFP+) PCs after a focal stroke to the sensorimotor cortex. Sham surgery mice (sham mice) contained GFP+ cells in the SVZ and subgranular zone of the dentate gyrus, in addition to a low density throughout the brain (Figure 1A), as reported in naive mice (Tanaka et al., 2009; Yamaguchi et al., 2000). At 1 week post stroke (1 wps), a pronounced increase in GFP+ cell density was observed within the lateral and ventral peri-infarct cortices (Figures 1B and 1D), and persisted solely in the ventral peri-infarct cortex at 4 weeks post stroke (4 wps) (Figures 1C and 1D).

Stroke can elicit a multilineage PC response (Li et al., 2010a, 2014), thus we phenotyped the GFP+ population in sham and stroke conditions. Similar to reports in naive

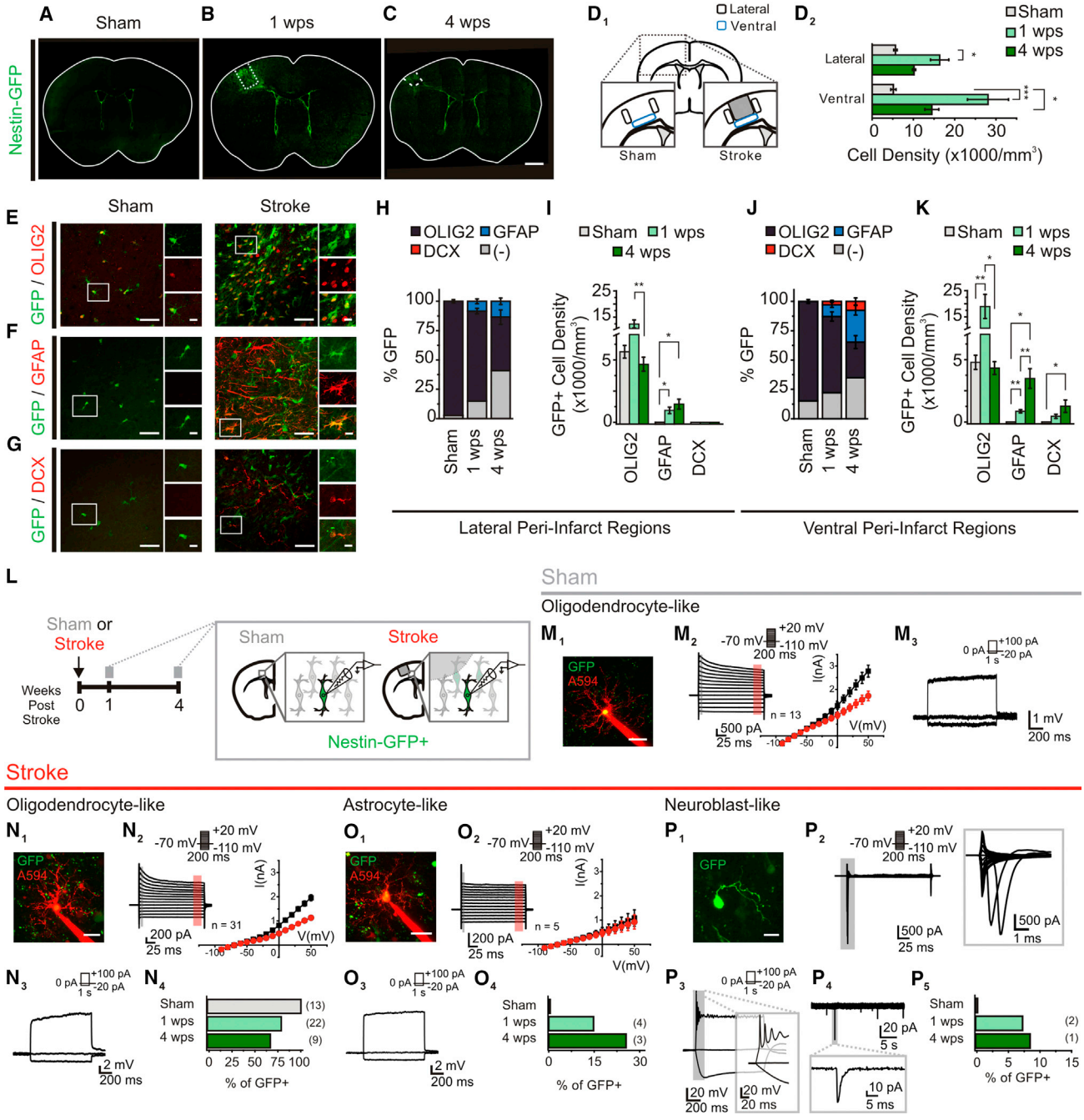

Figure 1. Cortical Stroke Induces a Spatial and Temporal Multilineage Response from Nestin-GFP Precursor Cells

(A–C) GFP cells in the Nestin-GFP mouse following sham surgery (A), or 1 week (1 wps) (B) and 4 weeks (4 wps) (C) after cortical stroke.

(D) Schematic of quantification regions in the sham and stroke-injured cortex (D1), and quantification of GFP+ cell density (D2). *$p < 0.05$; ***$p < 0.0005$; $p < 0.001$, Kruskal-Wallis test; n = 5 mice/group.

(E–G) Immunostained sham mouse cortex (left panel) and stroke-injured ventral peri-infarct cortex at 1 wps (right panel) of GFP with OLIG2 (E), GFAP (F), and DCX (G).

(H and I) Proportion (H) and density (I) of GFP+ cells in the lateral peri-infarct cortex. The proportion of GFP/OLIG2+ cells was ~97% in sham mice, and decreased post stroke. $p < 0.0001$; $p < 0.05$ versus 1 wps; $p < 0.0001$ versus 4 wps, one-way ANOVA. GFP/GFAP+ cells were only observed after stroke (1 wps: $p < 0.05$; 4 wps: $p < 0.05$, versus sham; one-sample t test versus test mean), but their proportion did not change between 1 and 4 wps. GFP/OLIG2+ density showed a non-significant increase at 1 wps (versus sham), with a significant decrease

(legend continued on next page)

mice (Tanaka et al., 2009), the majority of cortical GFP+ cells in sham mice expressed the oligodendrocyte marker OLIG2, but not the astrocytic marker glial fibrillary acidic protein (GFAP), or the immature neuronal marker doublecortin (DCX) (Figures 1E–1H and 1J). Ischemia provoked a prominent, but transient, increase in cortical GFP/OLIG2+ cell density in the ventral peri-infarct cortex (Figures 1E, 1I, and 1K), consistent with previous reports (Buffo et al., 2005). However, the proportion of GFP/OLIG2+ cells decreased after stroke (Figures 1H and 1J). Interestingly, two new GFP+ populations emerged in the cortex after stroke. A GFP/GFAP+ population was observed in both peri-infarct regions, consisting of ~8–27% of GFP+ cells between 1 and 4 wps (Figures 1F, 1J, and 1K). In addition, a GFP/DCX+ population was observed within the ventral peri-infarct region, comprising 2% and 8% of all GFP+ cells at 1 and 4 wps, respectively (Figures 1G, 1J, and 1K). Thus, our data support that a minor portion of the PC population develop into DCX+ immature neurons within the stroke-injured cortex.

To gain further insights into the identity of PCs post stroke, we examined excitability features of GFP+ cells in the peri-infarct cortex using whole-cell electrophysiology (Figure 1L). In sham mice, all GFP+ cells (13/13) displayed a 4AP-sensitive inactivating outward current (Figures 1M_2 and S1), suggesting the presence of an A-type potassium conductance. These cells had a low input resistance (IR), hyperpolarized resting membrane potential (RMP) (Table S1), and no overt signs of sodium conductances (Figure 1M_2), or action potential (AP) firing (Figure 1M_3). These properties are consistent with cortical NG2/OLIG2 oligodendrocytes (Chittajallu et al., 2004; Tanaka et al., 2009) and, when combined with our histological findings, suggest that the sham Nestin-GFP cortex contains a homogeneous population of GFP+ oligodendrocytes.

In sharp contrast to control conditions, the stroke-injured cortex contained an electrophysiologically heterogeneous cell population that could be broadly subdivided into three groups. First, we observed cells whose properties were largely analogous to those of the GFP/OLIG2+ cells in sham mice (Figures 1N_1–1N_3; Table S1). These cells were frequently observed approximately 1 wps, but less at 4 wps (Figure 1N_4). Second, we encountered cells with excitability features classically found in GFAP+ astrocytes (Steinhauser et al., 1992; Zhou et al., 2006): low IR, hyperpolarized RMPs (Table S1) and passive membrane behaviors (Figures 1O_1–1O_3). Their occurrence increased with time after stroke, reaching ~20% by 4 wps (Figure 1O_4). Last, we observed a small group of cells within ventral peri-infarct regions with a unique excitability profile suggestive of immature neurons (Figure 1P). They displayed a high IR (>2 GΩ), a depolarized RMP (Table S1), and clear signs of sodium conductances: fast inward currents in response to depolarizing steps (Figure 1P_2), and well-defined APs (Figure 1P_3). In a few instances

observed at 4 wps ($p < 0.01$ versus 1 wps; overall, $p = 0.001$, Kruskal-Wallis test). GFP/GFAP+ cells were only present post stroke (1 wps: $p < 0.05$; 4 wps: $p < 0.05$, versus sham; one-sample t test versus test mean). No GFP/DCX+ cells were observed (n = 3–7 mice/group).
(J and K) Proportion (J) and density (K) of GFP+ cell types in the ventral peri-infarct cortex. The proportion of GFP/OLIG2+ cells showed a trend toward decreasing at 1 wps ($p = 0.054$), and was significantly less at 4 wps ($p < 0.001$), in comparison with sham ($p < 0.0001$, one-way ANOVA). GFP/GFAP+ cells were only observed after stroke (1 wps: $p < 0.05$; 4 wps: $p < 0.01$, versus sham; one-sample t test versus test mean), and their proportion increased from 1 to 4 wps ($p < 0.05$, t test). GFP/DCX+ cells were only present post stroke (1 wps: $p < 0.05$; 4 wps: $p < 0.05$, versus sham; one-sample t test versus test mean). GFP/OLIG2+ density increased at 1 wps ($p = 0.01$; $p < 0.05$ versus sham), but returned to sham levels by 4 wps ($p < 0.05$, one-way ANOVA). GFP/GFAP+ cells only appeared post stroke (1 wps: $p < 0.01$; 4 wps: $p < 0.05$ versus sham; one-sample t test versus test mean), and their density increased from 1 to 4 wps ($p < 0.05$, t test). GFP/DCX+ cells only appeared post stroke (significant at 4 wps: $p < 0.05$ versus sham; one-sample t test versus test mean; n = 3–7 mice/group).
(L) Schematic of experiment.
(M) Properties of cortical GFP cells from sham mice. (M1) Two-photon (2P) image of a GFP cell filled with Alexa 594. (M2) Current traces responding to voltage steps, and I-V graph of the amplitude at 5 ms (black, black highlight on trace) and 180–190 ms (red, red highlight on trace) from voltage step onset. (M4) Voltage traces, responding to current steps.
(N) Properties of the first peri-infarct GFP population that resemble the cells observed in the sham cortex. (N1) 2P image of a GFP cell filled with Alexa 594. (N2) Current traces responding to voltage steps, and I-V graph of the amplitude at 5 ms (black, black highlight on trace) and 180–190 ms (red, red highlight on trace) from voltage step onset. (N3) Voltage traces, responding to current steps. (N4) Proportion of cells with observed electrophysiological phenotype.
(O) Properties of the non-excitable second GFP population. (D1) 2P image of a GFP cell filled with Alexa 594. (O2) Current traces responding to voltage steps, and I-V graph of the amplitude at 5 ms (black, black highlight on trace) and 180–190 ms (red, red highlight on trace) from voltage step onset. (O3) Voltage traces responding to current steps. (O4) Proportion of cells with observed electrophysiological phenotype.
(P) Properties of the excitable third GFP population. (P1) 2P image of a GFP cell. (P2) Current traces responding to voltage steps, showing fast inward current. (P3) Voltage traces, responding to current steps, showing the presence of APs. (P4) Current traces of sPSCs (Vh, −70 mV). (P5) Proportion of cells with observed electrophysiological phenotype.
Scale bars, 1 mm (mosaic) (A–C), 20 μm (insets); 40 μm (E–G), 10 μm (insets); 20 μm (M1, N1, and O1); 10 μm (P1). Data: mean ± SEM. See also Figure S1.

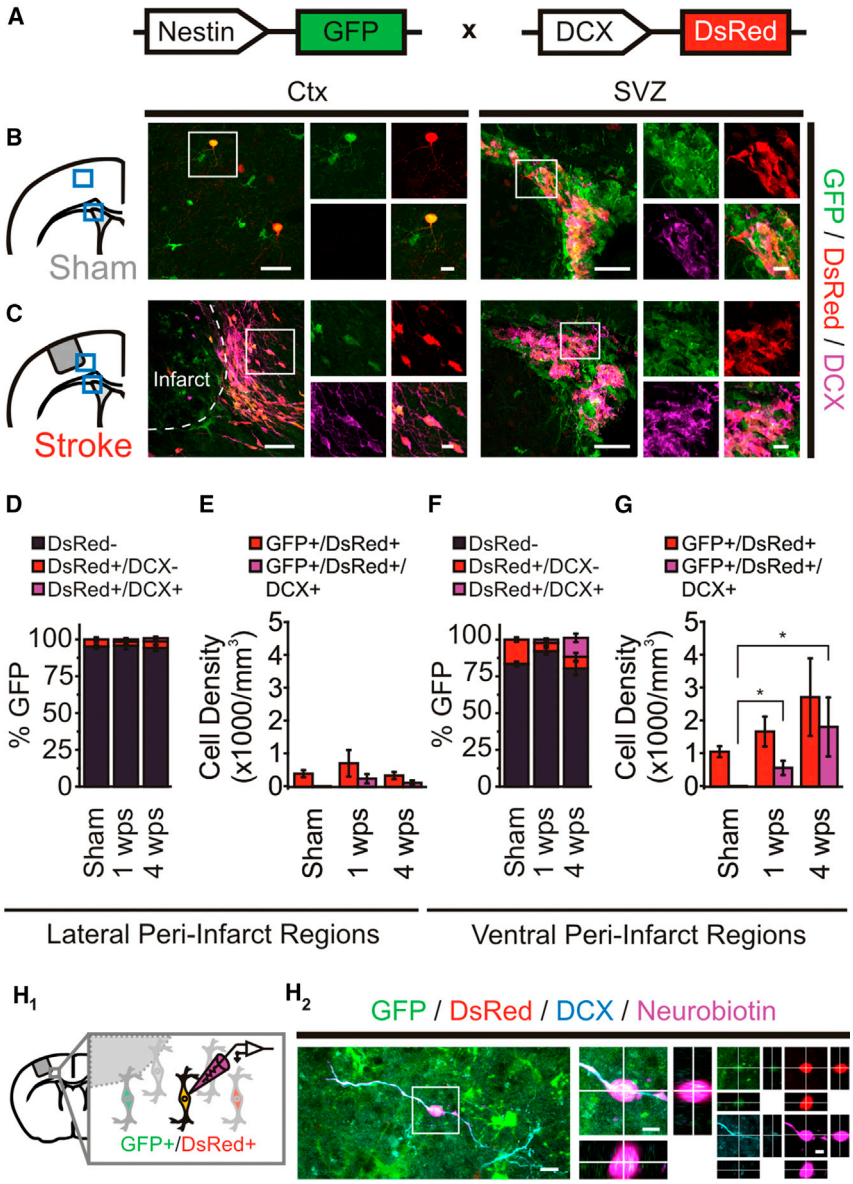

Figure 2. Nestin-GFP/DCX-DsRed Mice Identify Neuron-Fated Precursor Cells in the Stroke-Injured Cortex

(A) Schematic of Nestin-GFP/DCX-DsRed mouse.

(B) Immunostained sham brain with GFP+/DsRed+/DCX− cells in cortex and GFP+/DsRed+/DCX+ cells in the SVZ.

(C) Immunostained stroke-injured brain, with GFP+/DsRed+/DCX+ cells in ventral-peri-infarct cortex and the SVZ.

(D) Proportion of GFP+ cells in the lateral peri-infarct cortex.

(E) GFP/DsRed+ cell density in the lateral peri-infarct cortex.

(F) Proportion of GFP+ cells in the ventral peri-infarct cortex. GFP/DsRed/DCX+ cells were only present post stroke (1 wps: $p < 0.05$; 4 wps: $p < 0.05$, versus sham; one-sample t test versus test mean).

(G) GFP/DsRed+ cell density in the ventral peri-infarct cortex. GFP/DsRed/DCX+ cells were only present post stroke (1 wps: $p < 0.05$; 4 wps: $p < 0.05$, versus sham; one-sample t test versus test mean). n = 4–7 mice/group (D–G).

(H) GFP/DsRed+ cells in the ventral peri-infarct cortex co-express endogenous DCX. (H1) Schematic of whole-cell electrophysiological experiment performed on a peri-infarct GFP/DsRed+ cell filled with Neurobiotin (purple). (H2) *Post hoc* immunodetection of Neurobiotin, GFP, DsRed, and endogenous DCX in peri-infarct GFP/DsRed cell.

Scale bars, 40 μm (B and C), 10 μm (insets); 10 μm (H2), 5 μm (insets). Data: mean ± SEM. See also Figure S2.

(2/3 cells), infrequent spontaneous postsynaptic currents (sPSCs) were observed (Figure 1P$_4$). Many of these electrophysiological properties resemble those of SVZ-derived cells within the SVZ and rostral migratory stream (Belluzzi et al., 2003; Carleton et al., 2003; Wang et al., 2003). These properties, combined with their preferential localization, which corresponds to our analysis of the ventral peri-infarct region (Figures 1J and 1K), suggest that this last population represents the DCX+ immature neurons.

Nestin-GFP/DCX-DsRed Peri-infarct Cells Acquire a GABAergic Phenotype

The results outlined above led us to hypothesize that the excitable GFP+ cells present post stroke were the DCX+ immature neurons. To test this, and increase our capacity to identify DCX+ PCs for *ex vivo* recordings, we generated a Nestin-GFP/DCX-DsRed mouse line (Figure 2A). In the sham mouse cortex, a small proportion (~5%–10%) of GFP+ cells expressed DsRed (Figures 2B, 2D, and 2F), raising the concern that DsRed expression may occur independently of endogenous DCX, as reported in other rodent models (Trost et al., 2014). Consistent with this idea, no GFP/DsRed+ cells expressed endogenous DCX in the sham cortex, despite strong co-labeling in the SVZ (Figures 2B and 2D–2G). In contrast, endogenous DCX could be observed in cortical GFP/DsRed+ cells following stroke (Figure 2C). These GFP/DsRed/DCX+ cells were located primarily within the ventral region at 4 wps (Figures 2F and 2G)

and resembled DCX+ cells found in peri-infarct regions post stroke (Kunze et al., 2015; Osman et al., 2011). To confirm that immature neurons could be successfully targeted for electrophysiology experiments, a subset of GFP/DsRed+ cells were filled with Neurobiotin, and *post hoc* quadruple-label immunohistochemistry confirmed the co-expression of GFP, DsRed, Neurobiotin, and endogenous DCX (n = 6) (Figure 2H). GFP/DsRed+ cell density in the ventral region appeared to decrease at 8 wps (Figure S2), consistent with previous reports of DCX expression (Osman et al., 2011). Together, these results re-affirm that immature neurons localize throughout ventral peri-infarct cortex, and validate the Nestin-GFP/DCX-DsRed mouse as a tool to reliably identify and examine immature neurons in the cortex following stroke.

Previous reports have suggested that immature neurons found in the stroke-injured cortex predominantly originate from the SVZ (Osman et al., 2011). Indeed, the ventral peri-infarct GFP/DsRed population seemed to be SVZ derived, as pulse bromodeoxyuridine (BrdU) injections to label SVZ-PCs prior to stroke resulted in GFP/DsRed/BrdU+ cells in the ventral peri-infarct regions in stroke, but not sham mice (Figures S3A–S3C). In addition, retroviral infection of SVZ-PCs during stroke induction resulted in >60% of virally infected PCs in the ventral peri-infarct region to co-express DCX at 4 wps (Figures S3D–S3G).

As SVZ-PCs give rise to GABAergic interneurons (Luskin, 1993), we phenotyped GFP/DsRed+ cells at 4 wps for several neuronal markers (Figure 3A). Peri-infarct GFP/DsRed+ cells showed minor expression of calretinin and tyrosine hydroxylase (Figures 3C, 3D, and 3G), and no expression of calbindin or TBR1, a layer VI principal cell marker (Figures 3E–3G). However, a large portion (~85%) of these cells expressed glutamate decarboxylase (Figures 3B and 3G). Analysis of 4 wps GFP/DsRed+ cells using fluorescence-activated cell sorting (FACS) analysis and PCR further revealed that these peri-infarct cells expressed mRNA for interneuron markers (GAD65, GAD67, and VGAT), but not principal cells (VGlut1) (Figures 3H–3J), supporting our hypothesis that adult-generated immature neurons in the peri-infarct cortex are GABAergic cells.

Nestin-GFP/DCX-DsRed Peri-infarct Cells are Excitable Neurons with Functional GABAergic Synapses

Using this bitransgenic reporter mouse, we targeted GFP/DsRed+ cells localized to the ventral peri-infarct region for whole-cell electrophysiology at 4 wps. First, we encountered cells exhibiting outward non-inactivating currents in response to positive voltage steps, with little to no sign of fast inward currents, which we classified as class 1 (Figures $4A_1$ and $4B_1$). Direct current injection at times elicited small spike-like depolarizations (6/11 cells), but no bona fide APs (Figure $4C_1$). We next encountered cells displaying outward non-inactivating currents, but also displayed clear fast inward currents suggesting the presence of sodium channels (class 2; Figures $4A_2$ and $4B_2$). Small current injection (<10 pA) evoked at least one AP, with some cells sustaining short trains of APs, while increasing current step amplitudes lead to an unambiguous depolarization block (Figure $4C_2$). Last, we encountered cells that showed a prominent fast inward current, an A-type potassium-like conductance, with a conspicuous near absence of a non-inactivating outward conductance (class 3; Figures $4A_3$ and $4B_3$). Consistent with this conductance profile, direct current injection elicited single APs followed by large plateau potentials resembling depolarization block (Figure $4C_3$). The inherent inability of the transgenic reporter mouse to neither birthdate nor indelibly label cells limited our capacity to further study the source of the observed heterogeneity in excitability features of GFP/DsRed cells. These results, however, demonstrate the presence of multiple populations of immature excitable neurons in the peri-infarct cortex.

Next, to assay the capacity for functional integration, we examined the presence of synaptic inputs. We were unable to electrically evoke postsynaptic currents (PSCs) in class 1 (0/11), but PSCs were observed in both class 2 (3/23) and 3 (5/7) cells. These electrically evoked synaptic responses reversed at around −40 mV, consistent with a chloride conductance in our conditions (Figure 4D), and were blocked by the $GABA_A$ receptor antagonist bicuculline methiodide (Bic) (20 μm) (Figures 4E and 4F). Spontaneous (s) PSCs were present in the majority of class 1 cells (11/14), and in all class 2 (21/21) and class 3 (7/7) cells (Figure 4G). Whereas the sPSC frequency for all classes was notably low (~0.02–0.22 Hz, Figure $4H_2$; Table S2), their amplitudes were broadly similar (Figure $4H_1$; Table S2). The very low sPSC frequency precluded further sPSC characterization in class 1 cells; however, we observed that the sPSC frequency was greatly (~85%) reduced by Bic in class 2 and class 3 cells (Figures 4J and 4K). Collectively, our results demonstrate that GFP/DCX+ GABAergic immature neurons preferentially receive GABAergic synaptic input in the post stroke cortex. The scarcity of synaptic events, however, denotes the limited synaptic integration achieved by immature neurons into the damaged cortical network.

DISCUSSION

The ischemia-induced PC response is commonly suggested to contribute to stroke recovery (Lagace, 2012). Yet, the controversy regarding the neurogenic response post stroke, as well as the relative paucity of knowledge on the functional capacity of these cells, limits our understanding of this potential regenerative process. Here, we conduct a thorough

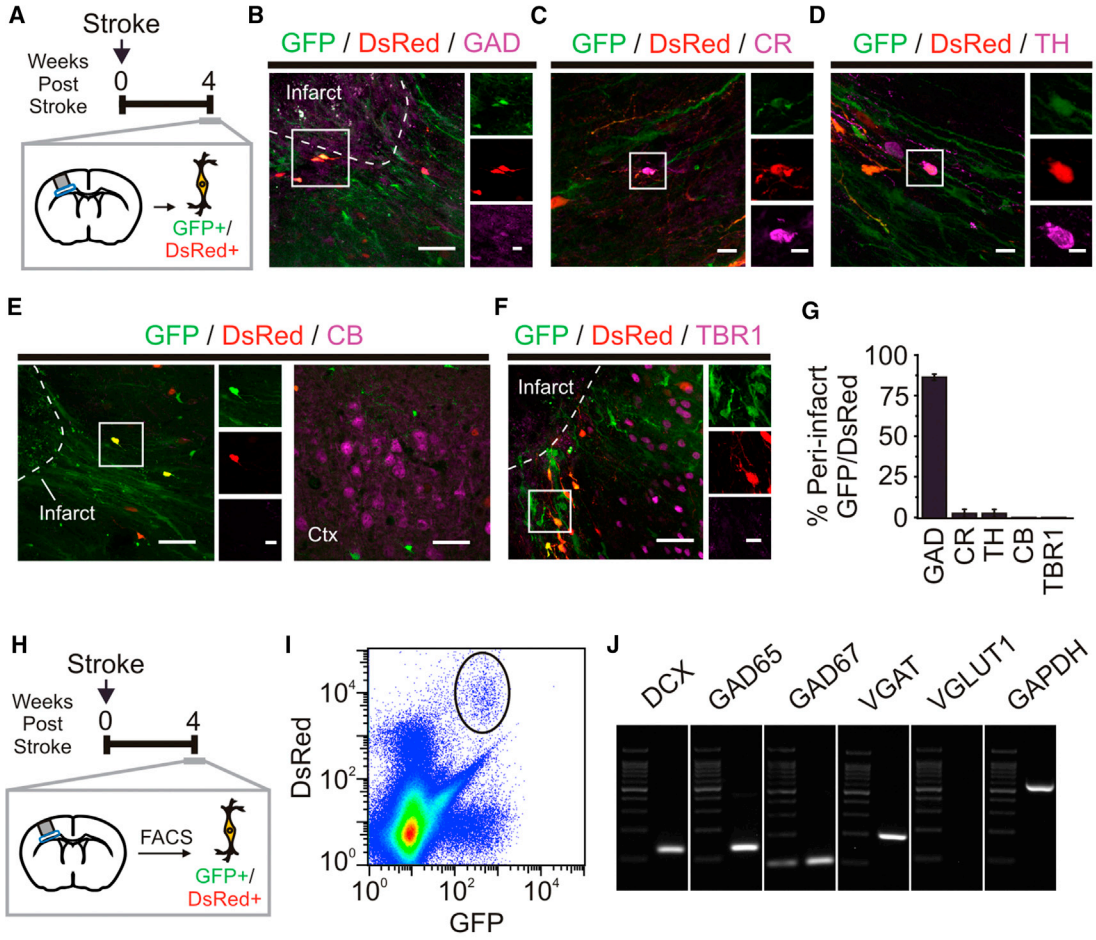

Figure 3. Peri-infarct GFP/DsRed+ Cells Express GABAergic Neuronal Markers in the Stroke-Injured Cortex

(A) Schematic of experiment on the ventral peri-infarct cortex at 4 wps.

(B–F) Immunostained ventral peri-infarct cortex at 4 wps, showing GFP/DsRed+ cell colabeled with GAD65/67 (GAD) (B), calretinin (CR) (C), tyrosine hydroxylase (TH) (D), but not calbindin (CB) (E) or TBR1 (F).

(G) Proportion of ventral peri-infarct GFP/DsRed+ cells expressing markers (n = 3–4 mice).

(H) Schematic of experiment performed to isolate GFP/DsRed+ cells from the ventral peri-infarct cortex at 4 wps.

(I and J) Density scatterplots of FACS-isolated cells reveal a GFP/DsRed+ population (solid black line) (I) and mRNA expression in FACS-isolated GFP/DsRed+ cells from the 4 wps ventral peri-infarct cortex (J) (pooled tissue from three mice).

Scale bars, 40 μm (B–F), 10 μm (insets). Data: mean ± SEM.

investigation of the PC response in the peri-infarct cortex after focal stroke. We reveal that cells with a neuronal lineage, while few in number, are unequivocally GABAergic neurons with the ability to fire APs. These neurons, however, receive sparse GABAergic synaptic innervation, indicative of an underdeveloped capacity to functionally integrate into an injured cortical network. Together, these findings show that the stroke-injured brain evokes a suboptimal endogenous neurogenic process to create functional GABAergic neurons in the injured brain.

Our results raise new hypotheses. First, the neurons encountered in the peri-infarct cortex after a stroke shared a number of functional features with SVZ-derived neuroblasts, granule cells, and periglomerular cells found in the adult olfactory bulb (Belluzzi et al., 2003; Carleton et al., 2003; Wang et al., 2003). This phenotypic resemblance raises the intriguing possibility that the recovering strategy of the ischemic cortex in essence relies on an ectopic re-routing of olfactory bulb-destined interneurons. If future studies were to convincingly establish the occurrence of this recovery process, it would oppose current theories that suggest that ischemia generates new neurons of subtypes normally resident in the damaged region, for instance as suggested in the stroke-injured striatum (Arvidsson et al., 2002; but see Liu et al., 2009; Parent et al., 2002).

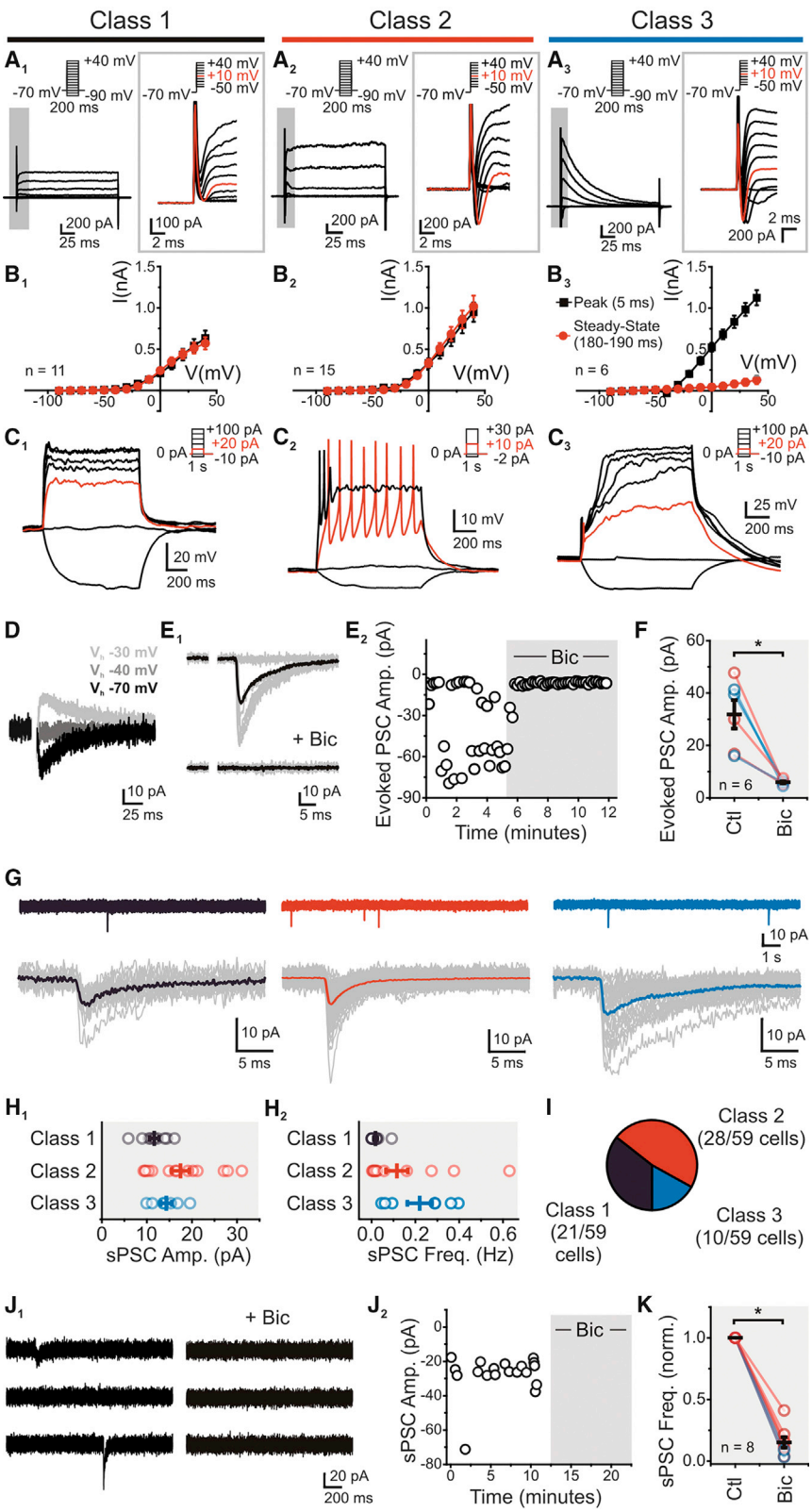

Figure 4. Peri-infarct Excitable Immature Neurons Acquire GABAergic Synaptic Input in the Stroke-Injured Cortex

(A–C) Properties of three unique classes of cortical GFP/DsRed+ cells post stroke. (A1–A3) Current traces resulting from voltage steps, with insets expanding on the 10 ms following depolarizing voltage steps. Significant inward currents were observed in both class 2 (A2) and class 3 (A3) cells. (B1–B3) I-V graphs of the amplitude 5 ms (black) and 180–190 ms (red) from voltage-step onset. (C1–C3) Voltage traces corresponding to current steps.

(D) Current traces of an evoked PSC, reversing at −40 mV.

(E) Traces (E1) and scatterplot (E2) of evoked PSC amplitude before and after application of bicuculline methiodide (Bic) (20 μM).

(F) Evoked PSCs in class 2 (red), class 3 (blue), and combined 2 and 3 (black) cells are blocked by Bic ($p < 0.01$, paired t test).

(G) Current traces of sPSCs (Vh, −70 mV), for class 1, 2 and 3. Lower panel, cell-averaged sPSC event from single voltage-clamp recordings (individual events in gray).

(H) Cell-averaged sPSC amplitude (H1) and frequency (H2) (n = 12 [class 1], 14 [class 2], 7 [class 3]).

(I) Proportion of peri-infarct GFP/DsRed+ cells showing one of three electrophysiological phenotypes, classified by voltage-step response.

(J) Traces (J1) and scatterplot (J2) of sPSCs before and after Bic application (20 μM).

(K) Cell-averaged sPSC frequency in class 2 (red), class 3 (blue), and combined 2 and 3 (black) cells showing that sPSCs frequency is blocked by Bic ($p < 0.05$, paired t test). Ctl., control; Amp., amplitude; Freq., frequency. Data: mean ± SEM.

Second, we encountered immature neurons that displayed a remarkably high IR, and readily fired APs, also unlike the adult-generated neurons described in the stroke-injured striatum (Hou et al., 2008). While the unique excitability profile of these adult-generated neurons could potentially facilitate and maximize their integration into the cortex, akin to what has been proposed to occur during the neurogenic process in the dentate gyrus (Gu et al., 2012; Schmidt-Hieber et al., 2004), their sparse synaptic innervation as demonstrated by their low sPSC frequency may be insufficient to incite substantial changes to a cortical network. As such, this work points to possible key limiting factors affecting the suboptimal endogenous neurogenic response present in the ischemic cortex. Our study of the excitability features and functional integration of adult-generated GABAergic neurons within the post stroke cortex reframes the challenge of stroke recovery toward increasing the number of neurons, and maximizing their incorporation, to ultimately impact behavioral recovery following stroke.

EXPERIMENTAL PROCEDURES

Mice and Surgical Procedures

Nestin-GFP (Yamaguchi et al., 2000) and DCX-DsRed (Couillard-Despres et al., 2006) mice were maintained in standard laboratory cages on a 12-hr light/dark cycle. Focal ischemia was produced in the sensorimotor cortex using a modified version of the photothrombotic model (Watson et al., 1985). Animal procedures were approved by the University of Ottawa Animal Care Committee and adhered to the guidelines set forth by the Canadian Council on Animal Care.

Histology

Mice were perfused with 4% paraformaldehyde, brains were stored in 30% sucrose (in 1× PBS) and sectioned (40 μm) with a Leica sliding microtome. Free-floating sections were processed for fluorescent immunohistochemistry as described previously (Ceizar et al., 2016). Cells were quantified in the peri-infarct cortical region, defined as a 250-μm-wide zone surrounding the necrotic border of the infarct. Cells in the corpus callosum were excluded from analysis.

Electrophysiology

Coronal slices (300 μm) containing the full extent of the infarct were generated using a Leica VT1000S microtome. Since photothrombotic infarcts transition to become a substantial plug of necrotic tissue at 4 wps, agar blocks (3%) were mounted behind the brain tissue to maintain slice integrity. Whole-cell electrophysiology using a potassium gluconate-based intracellular solution and two-photon *ex vivo* imaging was conducted as described previously (Lee et al., 2016).

FACS Analysis and PCR

Peri-infarct cortical regions were sorted using a MoFlo Astrios EQ (Beckman Coulter, Canada). mRNA was extracted using Arcturus Picopure RNA Isolation Kit (Applied Biosystems; Thermo Fisher). RT-PCR was completed using 300 pg mRNA and the OneStep RT-PCR kit (QIAGEN).

SUPPLEMENTAL INFORMATION

Supplemental Information includes Supplemental Experimental Procedures, three figures, and five tables and can be found with this article online at https://doi.org/10.1016/j.stemcr.2018.10.011.

AUTHOR CONTRIBUTIONS

T.S.K., J.C.B., and D.C.L. designed and interpreted the research. T.S.K. performed the experiments and analyzed the data. A.C. provided surgical technical support. Y.X. performed FACS analysis. J.S.D. generated the retrovirus. T.S.K., J.-C.B., and D.C.L. wrote the paper.

ACKNOWLEDGMENTS

We would like to thank all members of the Lagace and Béïque laboratories, specifically Keren Leviel Kumar, Angela Nguyen, Mathew Seegobin, and Danielle Dewar-Darch for animal colony maintenance, and Karl Schnalzer and Mikaël Ladouceur for technical assistance. We would like to thank the University of Ottawa Flow Cytometery core facility for technical assistance with FACS isolation and analysis. We also thank Dr. Dale Corbett, Dr. Melissa Snyder, and Sean Geddes for helpful discussions. T.S.K. is grateful for support from the Heart and Stroke Foundation of Canada and the Canadian Partnership for Stroke Recovery. J.C.B. is supported by a grant-in-aid from the Heart and Stroke Foundation and the Canadian Institute for Health Research. D.C.L. is supported by grants from the Canadian Partnership for Stroke Recovery and the Canadian Institute for Health Research.

Received: July 27, 2017
Revised: October 13, 2018
Accepted: October 15, 2018
Published: November 8, 2018

REFERENCES

Arvidsson, A., Collin, T., Kirik, D., Kokaia, Z., and Lindvall, O. (2002). Neuronal replacement from endogenous precursors in the adult brain after stroke. Nat. Med. *8*, 963–970.

Belluzzi, O., Benedusi, M., Ackman, J., and LoTurco, J.J. (2003). Electrophysiological differentiation of new neurons in the olfactory bulb. J. Neurosci. *23*, 10411–10418.

Benner, E.J., Luciano, D., Jo, R., Abdi, K., Paez-Gonzalez, P., Sheng, H., Warner, D.S., Liu, C., Eroglu, C., and Kuo, C.T. (2013). Protective astrogenesis from the SVZ niche after injury is controlled by Notch modulator Thbs4. Nature *497*, 369–373.

Brown, C.E., Boyd, J.D., and Murphy, T.H. (2010). Longitudinal in vivo imaging reveals balanced and branch-specific remodeling of mature cortical pyramidal dendritic arbors after stroke. J. Cereb. Blood Flow Metab. *30*, 783–791.

Buffo, A., Vosko, M.R., Erturk, D., Hamann, G.F., Jucker, M., Rowitch, D., and Gotz, M. (2005). Expression pattern of the transcription factor Olig2 in response to brain injuries: implications for neuronal repair. Proc. Natl. Acad. Sci. U S A *102*, 18183–18188.

Carleton, A., Petreanu, L.T., Lansford, R., Alvarez-Buylla, A., and Lledo, P.M. (2003). Becoming a new neuron in the adult olfactory bulb. Nat. Neurosci. *6*, 507–518.

Carmichael, S.T. (2016). Emergent properties of neural repair: elemental biology to therapeutic concepts. Ann. Neurol. *79*, 895–906.

Ceizar, M., Dhaliwal, J., Xi, Y., Smallwood, M., Kumar, K.L., and Lagace, D.C. (2016). Bcl-2 is required for the survival of doublecortin-expressing immature neurons. Hippocampus *26*, 211–219.

Chittajallu, R., Aguirre, A., and Gallo, V. (2004). NG2-positive cells in the mouse white and grey matter display distinct physiological properties. J. Physiol. *561*, 109–122.

Couillard-Despres, S., Winner, B., Karl, C., Lindemann, G., Schmid, P., Aigner, R., Laemke, J., Bogdahn, U., Winkler, J., Bischofberger, J., et al. (2006). Targeted transgene expression in neuronal precursors: watching young neurons in the old brain. Eur. J. Neurosci. *24*, 1535–1545.

Dancause, N., Barbay, S., Frost, S.B., Plautz, E.J., Chen, D., Zoubina, E.V., Stowe, A.M., and Nudo, R.J. (2005). Extensive cortical rewiring after brain injury. J. Neurosci. *25*, 10167–10179.

Ekonomou, A., Johnson, M., Perry, R.H., Perry, E.K., Kalaria, R.N., Minger, S.L., and Ballard, C.G. (2012). Increased neural progenitors in individuals with cerebral small vessel disease. Neuropathol. Appl. Neurobiol. *38*, 344–353.

Gu, Y., Arruda-Carvalho, M., Wang, J., Janoschka, S.R., Josselyn, S.A., Frankland, P.W., and Ge, S. (2012). Optical controlling reveals time-dependent roles for adult-born dentate granule cells. Nat. Neurosci. *15*, 1700–1706.

Harrison, T.C., Silasi, G., Boyd, J.D., and Murphy, T.H. (2013). Displacement of sensory maps and disorganization of motor cortex after targeted stroke in mice. Stroke *44*, 2300–2306.

Hou, S.W., Wang, Y.Q., Xu, M., Shen, D.H., Wang, J.J., Huang, F., Yu, Z., and Sun, F.Y. (2008). Functional integration of newly generated neurons into striatum after cerebral ischemia in the adult rat brain. Stroke *39*, 2837–2844.

Huttner, H.B., Bergmann, O., Salehpour, M., Racz, A., Tatarishvili, J., Lindgren, E., Csonka, T., Csiba, L., Hortobagyi, T., Mehes, G., et al. (2014). The age and genomic integrity of neurons after cortical stroke in humans. Nat. Neurosci. *17*, 801–803.

Jin, K., Wang, X., Xie, L., Mao, X.O., Zhu, W., Wang, Y., Shen, J., Mao, Y., Banwait, S., and Greenberg, D.A. (2006). Evidence for stroke-induced neurogenesis in the human brain. Proc. Natl. Acad. Sci. U S A *103*, 13198–13202.

Jin, K., Wang, X., Xie, L., Mao, X.O., and Greenberg, D.A. (2010). Transgenic ablation of doublecortin-expressing cells suppresses adult neurogenesis and worsens stroke outcome in mice. Proc. Natl. Acad. Sci. U S A *107*, 7993–7998.

Kunze, A., Achilles, A., Keiner, S., Witte, O.W., and Redecker, C. (2015). Two distinct populations of doublecortin-positive cells in the perilesional zone of cortical infarcts. BMC Neurosci. *16*, 20.

Lagace, D.C. (2012). Does the endogenous neurogenic response alter behavioral recovery following stroke? Behav. Brain Res. *227*, 426–432.

Lee, K.F., Soares, C., Thivierge, J.P., and Beique, J.C. (2016). Correlated synaptic inputs drive dendritic calcium amplification and cooperative plasticity during clustered synapse development. Neuron *89*, 784–799.

Li, L., Harms, K.M., Ventura, P.B., Lagace, D.C., Eisch, A.J., and Cunningham, L.A. (2010a). Focal cerebral ischemia induces a multilineage cytogenic response from adult subventricular zone that is predominantly gliogenic. Glia *58*, 1610–1619.

Li, S., Overman, J.J., Katsman, D., Kozlov, S.V., Donnelly, C.J., Twiss, J.L., Giger, R.J., Coppola, G., Geschwind, D.H., and Carmichael, S.T. (2010b). An age-related sprouting transcriptome provides molecular control of axonal sprouting after stroke. Nat. Neurosci. *13*, 1496–1504.

Li, H., Zhang, N., Lin, H.Y., Yu, Y., Cai, Q.Y., Ma, L., and Ding, S. (2014). Histological, cellular and behavioral assessments of stroke outcomes after photothrombosis-induced ischemia in adult mice. BMC Neurosci. *15*, 58.

Liu, F., You, Y., Li, X., Ma, T., Nie, Y., Wei, B., Li, T., Lin, H., and Yang, Z. (2009). Brain injury does not alter the intrinsic differentiation potential of adult neuroblasts. J. Neurosci. *29*, 5075–5087.

Luskin, M.B. (1993). Restricted proliferation and migration of postnatally generated neurons derived from the forebrain subventricular zone. Neuron *11*, 173–189.

Osman, A.M., Porritt, M.J., Nilsson, M., and Kuhn, H.G. (2011). Long-term stimulation of neural progenitor cell migration after cortical ischemia in mice. Stroke *42*, 3559–3565.

Parent, J.M., Vexler, Z.S., Gong, C., Derugin, N., and Ferriero, D.M. (2002). Rat forebrain neurogenesis and striatal neuron replacement after focal stroke. Ann. Neurol. *52*, 802–813.

Schmidt-Hieber, C., Jonas, P., and Bischofberger, J. (2004). Enhanced synaptic plasticity in newly generated granule cells of the adult hippocampus. Nature *429*, 184–187.

Shimada, I.S., Peterson, B.M., and Spees, J.L. (2010). Isolation of locally derived stem/progenitor cells from the peri-infarct area that do not migrate from the lateral ventricle after cortical stroke. Stroke *41*, e552–e560.

Sorrells, S.F., Paredes, M.F., Cebrian-Silla, A., Sandoval, K., Qi, D., Kelley, K.W., James, D., Mayer, S., Chang, J., Auguste, K.I., et al. (2018). Human hippocampal neurogenesis drops sharply in children to undetectable levels in adults. Nature *555*, 377–381.

Steinhauser, C., Berger, T., Frotscher, M., and Kettenmann, H. (1992). Heterogeneity in the membrane current pattern of identified glial cells in the hippocampal slice. Eur. J. Neurosci. *4*, 472–484.

Sun, C., Sun, H., Wu, S., Lee, C.C., Akamatsu, Y., Wang, R.K., Kernie, S.G., and Liu, J. (2013). Conditional ablation of neuroprogenitor cells in adult mice impedes recovery of poststroke cognitive function and reduces synaptic connectivity in the perforant pathway. J. Neurosci. *33*, 17314–17325.

Tanaka, Y., Tozuka, Y., Takata, T., Shimazu, N., Matsumura, N., Ohta, A., and Hisatsune, T. (2009). Excitatory GABAergic activation of cortical dividing glial cells. Cereb. Cortex *19*, 2181–2195.

Trost, A., Schroedl, F., Marschallinger, J., Rivera, F.J., Bogner, B., Runge, C., Couillard-Despres, S., Aigner, L., and Reitsamer, H.A. (2014). Characterization of dsRed2-positive cells in the doublecortin-dsRed2 transgenic adult rat retina. Histochem. Cell Biol. *142*, 601–617.

Wang, D.D., Krueger, D.D., and Bordey, A. (2003). Biophysical properties and ionic signature of neuronal progenitors of the postnatal subventricular zone in situ. J. Neurophysiol. *90*, 2291–2302.

Watson, B.D., Dietrich, W.D., Busto, R., Wachtel, M.S., and Ginsberg, M.D. (1985). Induction of reproducible brain infarction by photochemically initiated thrombosis. Ann. Neurol. *17*, 497–504.

Yamaguchi, M., Saito, H., Suzuki, M., and Mori, K. (2000). Visualization of neurogenesis in the central nervous system using nestin promoter-GFP transgenic mice. Neuroreport *11*, 1991–1996.

Zhang, R., Zhang, Z., Wang, L., Wang, Y., Gousev, A., Zhang, L., Ho, K.L., Morshead, C., and Chopp, M. (2004). Activated neural stem cells contribute to stroke-induced neurogenesis and neuroblast migration toward the infarct boundary in adult rats. J. Cereb. Blood Flow Metab. *24*, 441–448.

Zhou, M., Schools, G.P., and Kimelberg, H.K. (2006). Development of GLAST(+) astrocytes and NG2(+) glia in rat hippocampus CA1: mature astrocytes are electrophysiologically passive. J. Neurophysiol. *95*, 134–143.

Stem Cell Reports, Volume *11*

Supplemental Information

Excitable Adult-Generated GABAergic Neurons Acquire Functional Innervation in the Cortex after Stroke

Timal S. Kannangara, Anthony Carter, Yingben Xue, Jagroop S. Dhaliwal, Jean-Claude Béïque, and Diane C. Lagace

Supplemental Figures and Tables

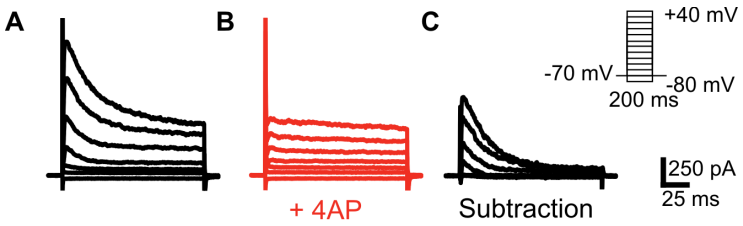

Figure S1. Nestin-GFP+ cell in the sham mouse cortex exhibit 4-AP sensitive currents. Related to Figure 1M. Example current traces recorded from a GFP+ cell in the sham surgery mouse cortex. (**A-B**) Current traces are in response to 200 ms voltage steps (-80 to +40 mV, Vh: -70 mV), prior to (**A**), and after 4AP (3mM) application (**B**). (**C**) Subtracted traces show the presence of a 4AP-sensitive early outward current (n = 3).

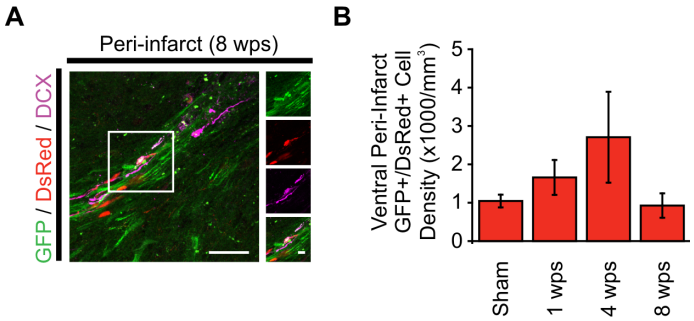

Figure S2. Decreased GFP/DsRed+ cell density in the cortex at 8 wps. Related to Figure 2. (**A**) Immunostained stroke-injured brain at 8 wps, with sparse GFP/DsRed/DCX+ cells in ventral-peri-infarct cortex (**B**) Density of cells expressing GFP/DsRed+ in the ventral peri-infarct cortex. n = 3-7 mice, Scale bars: 40 µm, 10 µm (insets). Data are represented as mean ± SEM.

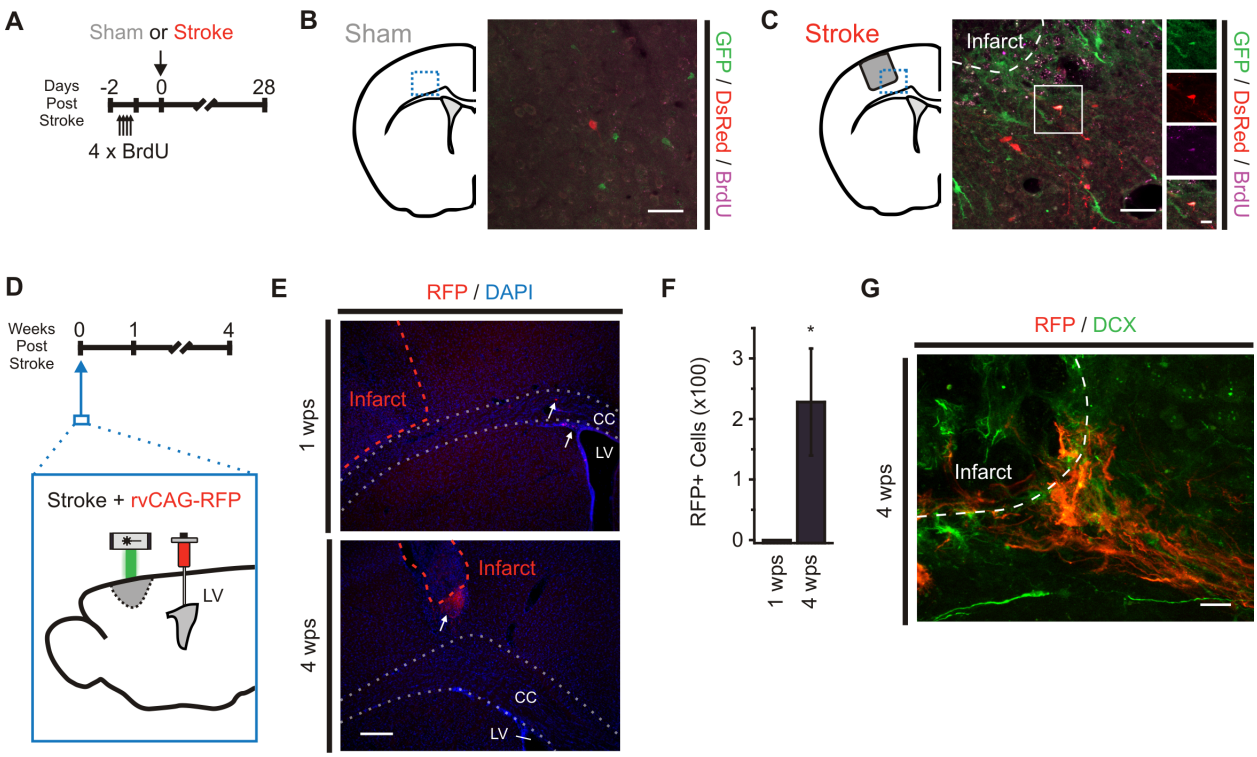

Figure S3. SVZ PCs contribute to DCX+ population at ventral peri-infarct regions. Related to Figure 2. (**A**) Schematic of experiment performed to label SVZ-PCs prior to stroke induction. (**B**) Immunostaining of sham surgery mouse cortex, four weeks after surgery. No GFP/DsRed/BrdU+ was detected (n=2). (**C**) Immunostaining of peri-infarct cortex, at 4 wps. A population of GFP/DsRed/BrdU+ could be detected (10.6 ± 5.3% of GFP/DsRed+ cells, n=4). (**D**) Schematic of experiment performed to label SVZ-PCs during stroke induction. (**E**) Immunostained stroke-injured brain, with RFP+ cells in the ventral peri-infarct cortex at 1 and 4 wps (**F**) Number of RFP+ cells identified at 1 and 4 wps in the peri-infarct cortex. (n = 2 (1 wps), 4 (4 wps), * indicates $p < 0.05$; One-Sample t-test vs. test mean) (**G**) Immunostained ventral peri-infarct cortex of a 4 wps mouse, with DCX detected in RFP+ cells. Scale bars: B, C = 40 µm, 10 µm (inset), E = 200 µm, G = 40 µm. Data are represented as mean ± SEM.

Table S1. Electrophysiological Properties of Nestin-GFP Precursor Cells in the Sham and Stroke-Injured Cortex. Related to Figure 1M-P.

GFP Cell Type	Input Resistance (IR; MΩ)	Resting Membrane Potential (RMP; mV)
Sham – Oligodendrocyte-type	58.6 ± 14.3 (n = 13)	-78.3 ± 1.8 (n = 13)
Stroke – Oligodendrocyte-type	289.1 ± 99.1 (n = 31)	-82.9 ± 1.1 (n = 30)
Stroke – Astrocyte-type	65.5 ± 7.0 (n = 7)	-82.8 ± 1.0 (n = 6)
Stroke – Neuron-type	3228.7 ± 1271.3 (n = 3)	-61.9 ± 6.2 (n = 3)

Table S2. Electrophysiological Properties of Nestin-GFP/DCX-DsRed Immature Neurons in the Stroke-Injured Cortex. Related to Figure 4.

GFP/DsRed Cell Type	Input Resistance (IR; MΩ)	Resting Membrane Potential (RMP; mV)	sPSC Amplitude (pA)	sPSC Frequency (Hz)
Class 1	6395.2 ± 803.0 (n = 21)	-56.7 ± 4.9 (n = 17)	11.6 ± 1.0 (n = 9)	0.02 ± 0.01 (n = 12)
Class 2	5346.8 ± 989.2 (n = 28)	-61.0 ± 4.7 (n = 20)	17.5 ± 2.0 (n = 14)	0.12 ± 0.05 (n = 14)
Class 3	6300.0 ± 1913.5 (n = 10)	-42.2 ± 5.8 (n = 5)	14.3 ± 1.2 (n = 7)	0.22 ± 0.06 (n = 7)

Table S3. Cells Recorded for Electrophysiological Experiments. Related to Figure 1M-P, Figure 4B, F, H, K

Figure	Experiment	# of Cells (# of Mice)
$1M_2$	IV curve	13 cells (6 mice)
$1N_2$	IV curve	31 cells (16 mice)
$1N_4$	% of GFP with oligodendrocyte-like properties	Sham: 13 cells (6 mice) 1 wps: 22 cells (8 mice) 4 wps: 9 cells (8 mice)
$1O_2$	IV curve	5 cells (4 mice)
$1O_4$	% of GFP with astrocyte-like properties	Sham: 0 cells 1 wps: 4 cells (2 mice) 4 wps: 3 cells (2 mice)
$1P_2$	% of GFP with neuron-like properties	Sham: 0 cells 1 wps: 2 cells (2 mice) 4 wps: 1 cell (1 mouse)
$4B_{1-3}$	IV curve	Class 1: 11 cells (9 mice) Class 2: 15 cells (13 mice) Class 3: 6 cells (6 mice)
4F	Evoked PSC Bicuculine	6 cells (5 mice)
$4H_1$	sPSC amplitude	Class 1: 9 cells (8 mice) Class 2: 14 cells (13 mice) Class 3: 7 cells (7 mice)
$4H_2$	sPSC frequency	Class 1: 12 cells (11 mice) Class 2: 14 cells (13 mice) Class 3: 7 cells (7 mice)
4K	sPSC Bicuculine	8 cells (6 mice)

Table S4. List of Antibodies/Primers Used. Related to Figures 1-3, S2-3.

Antibodies	Concentration Used	Source	Identifier
Chicken anti-GFP	1:5000 (mosaic images, whole-cell post hoc staining, BrdU staining, 1:50,000 for other experiments	Aves Labs	GFP-1020
Rabbit anti-DsRed	1:5000 (whole-cell post hoc staining, BrdU staining), no primary for other experiments	Clonetech	632496
Rabbit anti-OLIG2	1:500	Millipore	AB9610
Goat anti-Doublecortin	1:500	Santa Cruz	SC-8066
Mouse anti-GFAP	1:500	Millipore	MAB 3402
Mouse anti-Calretinin	1:5000	Millipore	MAB 1568
Rabbit anti-Tyrosine Hydroxylase	1:1000	Millipore	MAB 152
Rabbit anti-Calbindin	1:500	Millipore	AB1778
Rabbit anti-TBR1	1:1000	Abcam	AB31940
Rabbit anti-GAD65/67	1:500	Abcam	Ab11070
Rat anti-BrdU	1:500	AbCys	AbC117-7513
4′, 6-diamidine-2′-phenylindole dihydrochloride (DAPI)	1:10,000	Roche	10236276001
Donkey anti-Chicken CY2	1:500	Jackson Immuno.	703-546-155
Donkey anti-Rabbit CY3	1:500	Jackson Immuno.	711-585-152
Donkey anti-Goat CY3	1:500	Jackson Immuno.	705-165-147
Donkey anti-Mouse CY3	1:500	Jackson Immuno.	715-165-150
Donkey anti-Goat CY5	1:500	Jackson Immuno.	705-605-147
Donkey anti-Mouse CY5	1:500	Jackson Immuno.	715-605-150
Donkey anti-Rabbit CY5	1:500	Jackson Immuno.	711-175-152
Donkey anti-Rat CY5	1:500	Jackson Immuno.	712-175-153
Streptavidin CY5	1:200	Jackson Immuno.	016-170-084
Donkey anti-Goat Dylight 405	1:250	Jackson Immuno.	705-475-147

Gene	Genbank ID	Forward Primer (5′–3′) Reverse primer (5′–3′)	Fragment Size (bp)	Ref.
Dcx	NM_001110223	GAGTGCGCTACATTTATACCATTG TGACATTCTTGGTGTACTCAACCT	129	(Liu et al., 2009)
Gad2 (GAD65)	NM_008078.2	CATTGATAAGTGTTTGGAGCTAGCA GTGCGCAAACTAGGAGGTACAA	135	(Trifonov et al., 2014)
Gad1 (GAD67)	NM_008077	TCGATTTTTCAACCAGCTCTCTACT GTGCAATTTCATATGTGAACATATT	104	(Trifonov et al., 2014)
Slc32a1 (VGAT)	NM_009508	TCACGACAAACCCAAGATCAC GTCTTCGTTCTCCTCGTACAG	188	(Sgado et al., 2013)
Slc17a7 (VGLUT1)	NM_182993	CACAGAAAGCCCAGTTCAAC CATGTTTAGGGTGGAGGTAGC	155	(Sgado et al., 2013)
mGapdh	NM_008084	TCACCATCTTCCAGGAGCG CTGCTTCACCACCTTCTTGA	571	(Tanaka et al., 2018)

Table S5. Statistics for Figures 1-4, S4.

Figure	Type of Test	Output	P Value
1D2	Kruskal-Wallis Test	H(5) = 25.78	<0.0001
	Dunn's multiple comparison test	Lateral Sham vs. 1 wps	0.0342
		Lateral Sham vs. 4 wps	>0.9999
		Lateral 1 wps vs. 4 wps	0.8453
		Ventral Sham vs. 1 wps	0.0004
		Ventral Sham vs. 4 wps	0.0381
		Ventral 1 wps vs. 4 wps	>0.9999
1H: OLIG2	One-Way ANOVA	F(2,10) = 30.64	<0.0001
	Bonferroni Post hoc	Sham vs. 1 wps	0.0402
		Sham vs. 4 wps	<0.0001
		1 wps vs. 4 wps	0.0012
1H: GFAP	One Sample t-Test with Test Mean	1wps: t(3) = 4.0777	0.0266
		4 wps: t(3) = 4.965	0.0157
	Two Sample t-Test	1 wps vs. 4 wps: t(6) = -1.506	0.1824
1I: OLIG2	Kruskal-Wallis Test	H(2) = 9.284	0.0010
	Dunn's multiple comparison tests	Sham vs. 1 wps	0.2364
		Sham vs. 4 wps	>0.9990
		1 wps vs. 4 wps	0.0080
1I: GFAP	One Sample t-Test with Test Mean	1wps: t(3) = 3.676	0.0349
		4 wps: t(3) = 3.713	0.0340
	Two Sample t-Test	1 wps vs. 4 wps: t(6) = -1.070	0.3259
1J: OLIG2	One-Way ANOVA	F(2,10) = 33.41	<0.0001
	Bonferroni Post hoc	Sham vs. 1 wps	0.0536
		Sham vs. 4 wps	<0.0001
		1 wps vs. 4 wps	0.0006
1J: GFAP	One Sample t-Test with Test Mean	1wps: t(3) = 4.329	0.0160
		4 wps: t(3) = 6.614	0.0070
	Two Sample t-Test	1 wps vs. 4 wps: t(6) = -3.629	0.012
1J: DCX	One Sample t-Test with Test Mean	1wps: t(4) = 3.172	0.0338
		4 wps: t(6) = 2.614	0.0399
	Two Sample t-Test	1 wps vs. 4 wps: t(10) = -1.336	0.2119
1K: OLIG2	One-Way ANOVA	F(2,10) = 7.550	0.0100
	Bonferroni Post hoc	Sham vs. 1 wps	0.0420
		Sham vs. 4 wps	1.000
		1 wps vs. 4 wps	0.0160
1K: GFAP	One Sample t-Test with Test Mean	1wps: t(3) = 6.628	0.0070
		4 wps: t(3) = 4.450	0.0211
	Two Sample t-Test	1 wps vs. 4 wps: t(6) = -3.317	0.0161
1K: DCX	One Sample t-Test with Test Mean	1wps: t(4) = 2.745	0.0517
	Two Sample t-Test	4 wps: t(6) = 2.561	0.0428
		1 wps vs. 4 wps: t(10) = -1.341	0.2095
2D: DsRed-	Kruskal-Wallis test	H(2) = 0.7097	0.7237
2D: DsRed+/DCX-	Kruskal-Wallis test	H(2) = 1.186	0.5809
2D: DsRed+/ DCX+	One Sample t-Test with Test Mean	1wps: t(3) = 1.517	0.1132
		4 wps: t(6) = 1.222	0.1334
	Two Sample t-Test	1 wps vs. 4 wps: t(9) = -0.8223	0.4321
2E: GFP+/ DsRed+	Kruskal-Wallis test	H(2) = 0.2045	0.9187

2E: GFP+/DsRed+/ DCX+	One Sample t-Test with Test Mean Two Sample t-Test	1wps: t(3) = 1.617 4 wps: t(6) = 1.409 1 wps vs. 4 wps: t(9) = 0.8994	0.1021 0.1043 0.3919
2F: DsRed-	Kruskal-Wallis test	H(2) = 5.318	0.0597
2F: DsRed+/ DCX-	One-Way ANOVA	F(2,11) = 3.532	0.0654
2F: DsRed+/DCX+	One Sample t-Test with Test Mean Two Sample t-Test	1wps: t(3) = 2.823 4 wps: t(6) = 2.865 1 wps vs. 4 wps: t(9) = -1.897	0.0333 0.0143 0.0903
2G: GFP+/DsRed+	Kruskal-Wallis test	H(2) = 0.5327	0.7823
2G: GFP+/DsRed+/ DCX+	One Sample t-Test with Test Mean Two Sample t-Test	1wps: t(3) = 2.529 4 wps: t(6) = 2.003 1 wps vs. 4 wps: t(9) = -1.018	0.0427 0.0461 0.3355
4H1: Amp. of sPSCs	Kruskal-Wallis test	H(2) = 3.768	0.1520
4H2: Freq. of sPSCs	Kruskal-Wallis Test Dunn's multiple comparison tests	H(2) = 12.77 Class 1 vs. 2 Class 1 vs. 3 Class 2 vs. 3	0.0017 0.1812 0.0011 0.1186
4F	Paired Sample t-Test	t(5) = 4.700	0.0053
4K	Paired Sample t-Test	t(7) = 2.865	0.0242
S4F	One Sample t-Test with Test Mean	t(3) = 3.586	0.0186

Supplemental Experimental Procedures

Animals. Mice (5-9 weeks old) were group housed in standard laboratory cages and maintained on a 12-hour light/dark cycle with access to food and water ad libitum. Nestin-GFP (B6.Cg-Tg(Nes-EGFP)1Yamm) (Yamaguchi et al., 2000), DCX-DsRed (Couillard-Despres et al., 2006) were genotyped based on previously published protocols. Breeding homozygous Nestin-GFP and DCX-DsRed mice generated the bi-transgenic reporter mice line (Nestin-GFP/DCX-DsRed). Animal procedures were approved by the University of Ottawa Animal Care Committee and adhered to the guidelines set forth by the Canadian Council on Animal Care.

Photothrombosis. Focal ischemic infarcts were produced using a modified version of the photothrombotic stroke model (Watson et al., 1985). Briefly, mice were anesthetized with 1.5-2% isofluorane and fitted to a stereotaxic apparatus. Body temperature was maintained at 37.0 ± 1.0^{o}C. Mice received a single intraperitoneal injection of 1% Rose Bengal dye (sc-203757; 100 mg/kg, in 1x PBS). After 5 minutes, the exposed skull above the sensorimotor cortex (+1 mm anterior/posterior, +2.7 mm medial/lateral to bregma) was illuminated with a green laser beam generated by a diode pumped solid-state laser (~20mW, 532 nm, Beta Electronics) for 10 minutes. Sham animals received Rose Bengal administration without laser exposure.

Retrovirus Injection. Retrovirus generation and stereotaxic injection was performed as previously described (Ceizar et al., 2016; Tashiro et al., 2006). The CAG-RFP retroviral vector, and corresponding packing and envelope construct, was generously provided by Dr. Fred Gage (The Salk Institute, La Jolla, CA, USA). RFP virus titer was determined by live tittering using 293T cells and was measured to be 1.2×10^{9} infectious units (IU) per ml. RFP virus (1.5 µl) was stereotaxically injected (0.2 µl/minute) into the apex of the SVZ (-0.7 mm anterior/posterior, +1.2 mm medial/lateral, -1.9 mm dorsal/ventral to bregma) using a 33G needle (model: 7803-05) and 10 µl gastight microsyringe (model: 1700), attached to a Hamilton (Hamilton Company). Injection was performed approximately 10 minutes following photothrombotic stroke induction.

Bromodeoxyuridine (BrdU) Injection. Pulse BrdU injections were performed as previously described (Dhaliwal et al., 2015). Mice received four intraperitoneal injections of 50 mg/kg BrdU (10 mg/mL dissolve in saline; Fluka Analytical, Sigma- Aldrich Chemie), with each injection spaced by three hours. Two days later, mice received either a sham or stroke surgery.

Tissue Collection. Mice were anesthetized with Euthanyl and transcardially perfused with cold 1x PBS and 4% paraformaldehyde (in 1x PBS) at ~ 7 mL/minute. Brains were removed, post-fixed in 4% paraformaldehyde for 1 hour, and then placed in 30% sucrose (in 1x PBS) at 4^{o}C. Coronal tissue sections (40 µm) were generated with a Leica SM 2000 R sliding microtome (Leica Microsystems), and stored as a 1:9 series, in 1x PBS (with 0.01% sodium azide) at 4^{o}C.

Immunohistochemical Detection. Free-floating sections were processed for fluorescent immunohistochemistry as previously published (Ceizar et al., 2016; Dhaliwal et al., 2015), using primary and secondary antibodies listed in the **Table S4**. Briefly, sections were washed in 1x PBS (3 x 5 minutes), and incubated in 0.1% Tween-20 and 0.1% TritonX-100 in 1x PBS with corresponding primary antibodies, on a shaker at 4^{o}C, overnight. The following day, sections were washed in 1x PBS (3 x 5 minutes), and incubated in 0.1% Tween-20 and 0.1% TritonX-100 in 1x PBS with corresponding secondary antibodies, on a shaker at room temperature, for one to two hours. Sections were counterstained with the nuclear counterstain DAPI (4′, 6-diamidine-2′-phenylindole dihydrochloride) for 2.5 minutes to aid visualization. Alterations to the set protocol were made for 1) BrdU immunodetection experiments, where an acid pre-treatment step (1N HCl in 1x PBS, at 45^{o}C for 30 minutes(Kee et al., 2007)), and 1xPBS wash (3 x 5 minutes) were performed prior to primary antibody incubation, and DAPI counterstaining was extended to a five minute incubation, and 2) the quadruple-labeling experiment, where the goat anti-doublecortin antibody was visualized using a secondary conjugated to Dylight 405, and DAPI counterstaining was excluded. Sections were mounted onto Superfrost microscope slides and coverslipped with Immunomount (Fisher Scientific).

Imaging and Histological Quantification of Fluorescent Cells. Cells were quantified in the peri-infarct region, defined as a 250 µm wide zone surrounding the necrotic border of the infarct. Counting and co-localization was performed by semi-randomly placing four sampling boxes (210 x 210 µm) in the four regions surrounding the infarct. Cells in the corpus callosum were excluded from analysis. For each sampling box, confocal image stacks

using a Zeiss LSM510/AxioImager.M1 confocal microscope with a 40x oil immersion objective (N.A. = 1.3) were collected (optical slice: 1 μm at minimum; sequential excitation at 488, 543 and 633 nm). To image quadruple-labeled cells, a Zeiss LSM510 META/AxioVert 200 confocal microscope with a 40x oil objective (N.A. = 1.3) was used (optical slice: 1 μm at minimum; sequential excitation at 405, 488, 543 and 633 nm). For tile-scanned image in Figure 1A-C, tiles were acquired using a Zeiss LSM800/AxioObserver Z1 confocal microscope with a 10x objective (N.A. = 0.3).

Fluorescence-Activated Cell Sorting (FACS) Analysis and PCR. Nestin-GFP/DCX-DsRed mice were deeply anesthetized with isofluorane (Baxter Corporation, Canada). Mice were then decapitated, and their brains were placed in oxygenated artificial cerebrebrospinal fluid used for FACS (FACS-aCSF), consisting of (in mM): 124 NaCl, 5 KCl, 1.3 MgCl2 · 6H2O, 2 CaCl2 · 2H2O, 26 NaHCO3, and 1X penicillin-streptomycin (10,000 U/mL; ThermoFisher) (pH = 7.4). Coronal sections (1.0 mm) were generated using an Adult Mouse Brain Slicer Matrix (Zivic Instruments) and sterile razor blades. Cortical regions neighbouring the stroke-induced infract were isolated using a sterile scalpel and a Zeiss SteREO Discovery.V8 dissecting scope, transferred to eppendorf tubes with minimal amount of FACS-aCSF, and gently chopped using a sterile scalpel blade. Tissue was spun down and incubated (ten minutes, 37^{o}C) in 500 uL/tube of digestion media, containing: 20 U/mL papain (Worthington Biochemicals), 12 mM EGTA (Invitrogen) in DMEM:F12 (Invitrogen). Following incubation, Resuspension Media (0.05 mg/mL DNase1 (Roche), 10% fetal bovine serum (Wisent Bioproducts) in DMEM:F12 phenol-free medium) was added to each tube and incubated for five minutes. Supernatant was then transferred in Percoll media, consisting of 19.8% Percoll (GE Healthcare Life Sciences), 2.2% 10xPBS (Wisent Bioproducts) in Resuspension Media. Cells were then spun down (500 x g, 12.5 minutes, 4^{o}C), dissolved in DMEM:F12 phenol-free medium, and sorted using a MoFlo Astrios EQ (Beckman Coulter Canada) for GFP(488-526 nm) and DsRed (561-579 nm). mRNA was extracted using Arcturus Picopure RNA Isolation Kit (Applied Biosystems; ThermoFisher) and examined for quality and quantity using an AATI Fragment Analyzer (Advanced Analytical Technologies, Inc.). Primers used for amplification are listed in **Table S4**, and were purchased from Integrated DNA Technologies, Inc. RT-PCR was completed using 300 pg mRNA and the OneStep RT-PCR kit (Qiagen, Inc.).

Whole-Cell Electrophysiology. Whole-cell electrophysiology was performed as previously described (Geddes et al., 2016; Kannangara et al., 2015; Lee et al., 2016). Mice were deeply anesthetized with isofluorane (Baxter Corporation, Canada), and transcardially perfused with ice-cold, oxygenated choline-based artificial cerebrebrospinal fluid (choline-aCSF), containing the following: 119 choline-Cl, 2.5 KCl, 4.3 MgSO4, 1.0 NaH2PO4, 1.0 CaCl2, 11 glucose, and 26.2 NaHCO3 (pH 7.2-4). Mice were then decapitated and the brain was quickly removed. Coronal slices (300 μm), containing the full extent of the infarct, were generated using a Leica VT1000 S vibratome blade microtome (Leica Microsystems). Since photothrombotic infarcts transition to become a substantial plug of necrotic tissue by four weeks post stroke, agar blocks (3%) were mounted behind the brain tissue to maintain slice integrity during the slicing procedure. Brain sections were then transferred to an incubation chamber, and allowed to recover for at least 1 hour in oxygenated artificial cerebrospinal fluid (aCSF), containing the following: 119 NaCl, 2.5 KCl, 1.3 MgSO4, 1.0 NaH2PO4, 2.5 CaCl2, 11 glucose, and 26.2 NaHCO3 (pH = 7.2-4) initially maintained at 30^{o}C, then recovered at room temperature. Slices were transferred to a perfusion chamber and perfused with oxygenated aCSF (2 mL/minute) at room temperature. Borosilicate recording pipettes (4-8 MΩ, World Precision Instruments), pulled with a PC-10 pipette puller (Narishige, Japan) were backfilled with a potassium-based intracellular solution contained the following (in mM): 115 K-gluconate, 20 KCl, 10 HEPES, 4 Mg-ATP, 0.5 tris-GTP (Na salt hydrate) and 10 Na-phosphocreatine (pH 7.23-25, adjusted with KOH; 280–290 mOsm/L). In some experiments, the internal solution was supplemented with either the fluorophore Alexa 594 hydrazide (A10438; 0.03 mM, Na-salt, Molecular Probes) or Neurobiotin (SP-1120-50; 3 mM, Vector Laboratories). Cells were targeted using a Zeiss Axio Examiner D1 upright microscope using either a 20x (1.0 NA) or 40x (1.0 NA) objective. For voltage clamp recordings, we monitored access resistance by applying a 100 ms, 5 mV hyperpolarizing pulse prior to each sweep. Recordings were discarded if access resistance changed by > 30%. Liquid junction potentials were not compensated for. To measure post-synaptic currents (PSCs), single square pulses (100 μs) were evoked with an aCSF-filled borosilicate pipette (3-4 MΩ, World Precision Instruments), driven by an ISO-flex stimulation isolation unit (A.M.P.I), at 0.1 Hz. Spontaneous post-synaptic currents (sPSCs) were recording at -70 mV in normal aCSF. In some experiments, we bath applied -(-) bicuculline methiodide (Bic, ab120108; 20 μm, Abcam) to block $GABA_AR$-mediated currents. For a subset of experiments, two-photon imaging was performed to visualize the morphology of cell types. Imaging was conducted using a Ti:Sapphire pulsed laser tuned to 850 nm (MaiTai-DeepSee, Spectra Physics) coupled to a Zeiss LSM710 multiphoton microscope with a 20x (1.0 NA) objective.

Data and Statistical Analysis. All electrophysiological recordings were analyzed using Clampfit (Molecular Devices) and OriginPro 8.5 (OriginLab). sPSCs were analyzed using a sPSC current-template search through Clampfit. Results were processed using Microsoft Excel and statistical analysis was conducted using OriginPro 8.5 and GraphPad Prism 6 (Graphpad Software). For all studies, data was presented as mean ± standard error of the mean (SEM). Single variable data was analyzed using either a one-sample t-test (when comparing to a group that had a variance = 0) or a two-tailed two-sample student's t-test, while analysis for more than one variable was analyzed using an Analysis of variance (ANOVA) followed by a Bonferroni post hoc test. Data sets failing ANOVA assumptions were analyzed using Kruskal-Wallis tests with Geisser Greenhouse corrections, and Dunn's multiple comparison tests. Differences were considered to be statistically significant when $p < 0.05$. Statistical tests are reported in **Table S5**.

Supplemental References

Ceizar, M., Dhaliwal, J., Xi, Y., Smallwood, M., Kumar, K.L., and Lagace, D.C. (2016). Bcl-2 is required for the survival of doublecortin-expressing immature neurons. Hippocampus *26*, 211-219.

Couillard-Despres, S., Winner, B., Karl, C., Lindemann, G., Schmid, P., Aigner, R., Laemke, J., Bogdahn, U., Winkler, J., Bischofberger, J.*, et al.* (2006). Targeted transgene expression in neuronal precursors: watching young neurons in the old brain. Eur J Neurosci *24*, 1535-1545.

Dhaliwal, J., Xi, Y., Bruel-Jungerman, E., Germain, J., Francis, F., and Lagace, D.C. (2015). Doublecortin (DCX) is not Essential for Survival and Differentiation of Newborn Neurons in the Adult Mouse Dentate Gyrus. Front Neurosci *9*, 494.

Geddes, S.D., Assadzada, S., Lemelin, D., Sokolovski, A., Bergeron, R., Haj-Dahmane, S., and Beique, J.C. (2016). Target-specific modulation of the descending prefrontal cortex inputs to the dorsal raphe nucleus by cannabinoids. Proc Natl Acad Sci U S A *113*, 5429-5434.

Kannangara, T.S., Eadie, B.D., Bostrom, C.A., Morch, K., Brocardo, P.S., and Christie, B.R. (2015). GluN2A-/- Mice Lack Bidirectional Synaptic Plasticity in the Dentate Gyrus and Perform Poorly on Spatial Pattern Separation Tasks. Cereb Cortex *25*, 2102-2113.

Kee, N., Teixeira, C.M., Wang, A.H., and Frankland, P.W. (2007). Preferential incorporation of adult-generated granule cells into spatial memory networks in the dentate gyrus. Nat Neurosci *10*, 355-362.

Lee, K.F., Soares, C., Thivierge, J.P., and Beique, J.C. (2016). Correlated Synaptic Inputs Drive Dendritic Calcium Amplification and Cooperative Plasticity during Clustered Synapse Development. Neuron *89*, 784-799.

Liu, X.S., Chopp, M., Zhang, X.G., Zhang, R.L., Buller, B., Hozeska-Solgot, A., Gregg, S.R., and Zhang, Z.G. (2009). Gene profiles and electrophysiology of doublecortin-expressing cells in the subventricular zone after ischemic stroke. J Cereb Blood Flow Metab *29*, 297-307.

Sgado, P., Genovesi, S., Kalinovsky, A., Zunino, G., Macchi, F., Allegra, M., Murenu, E., Provenzano, G., Tripathi, P.P., Casarosa, S.*, et al.* (2013). Loss of GABAergic neurons in the hippocampus and cerebral cortex of Engrailed-2 null mutant mice: implications for autism spectrum disorders. Exp Neurol *247*, 496-505.

Tanaka, K.I., Xue, Y., Nguyen-Yamamoto, L., Morris, J.A., Kanazawa, I., Sugimoto, T., Wing, S.S., Richards, J.B., and Goltzman, D. (2018). FAM210A is a novel determinant of bone and muscle structure and strength. Proc Natl Acad Sci U S A.

Tashiro, A., Sandler, V.M., Toni, N., Zhao, C., and Gage, F.H. (2006). NMDA-receptor-mediated, cell-specific integration of new neurons in adult dentate gyrus. Nature *442*, 929-933.

Trifonov, S., Yamashita, Y., Kase, M., Maruyama, M., and Sugimoto, T. (2014). Glutamic acid decarboxylase 1 alternative splicing isoforms: characterization, expression and quantification in the mouse brain. BMC Neurosci *15*, 114.

Watson, B.D., Dietrich, W.D., Busto, R., Wachtel, M.S., and Ginsberg, M.D. (1985). Induction of reproducible brain infarction by photochemically initiated thrombosis. Ann Neurol *17*, 497-504.

Yamaguchi, M., Saito, H., Suzuki, M., and Mori, K. (2000). Visualization of neurogenesis in the central nervous system using nestin promoter-GFP transgenic mice. Neuroreport *11*, 1991-1996.